

# Role of Magnesium Silicates in Wet-Kneaded Silica–Magnesia Catalysts for the Lebedev Ethanol-to-Butadiene Process

Sang-Ho Chung,<sup>†,§</sup> Carlo Angelici,<sup>†,§</sup> Stijn O.M. Hinterding,<sup>†</sup> Markus Weingarth,<sup>‡</sup> Marc Baldus,<sup>‡</sup> Klaartje Houben,<sup>‡</sup> Bert M. Weckhuysen,<sup>\*,†</sup> and Pieter C.A. Bruijninx<sup>\*,†</sup>

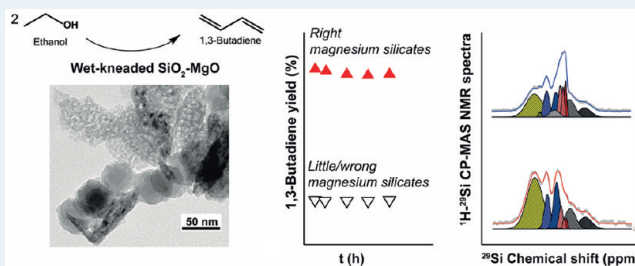
<sup>†</sup>Inorganic Chemistry and Catalysis, Debye Institute for Nanomaterials Science, Utrecht University, Universiteitsweg 99, 3584 CG Utrecht, The Netherlands

<sup>‡</sup>NMR Spectroscopy Research Group, Bijvoet Center for Biomolecular Research, Utrecht University, Padualaan 8, 3584 CH Utrecht, The Netherlands

## S Supporting Information

**ABSTRACT:** Wet-kneading is a technique commonly used for the synthesis of SiO<sub>2</sub>–MgO catalysts for the Lebedev ethanol-to-butadiene process, with catalyst performance known to depend heavily on the preparation parameters used in this method. Here, the large influence of Mg precursor and MgO content on morphology, chemical structure (as determined by TEM(-EDX), FT-IR, XRD and solid-state <sup>1</sup>H–<sup>29</sup>Si cross-polarized MAS NMR), and on catalyst performance is demonstrated. The Mg precursor used is found to influence the extent of magnesium silicate formation during wet-kneading, as estimated from TEM and FT-IR, which, in turn, was found to correlate with catalyst performance. Accordingly, the catalyst synthesized from a nanosized Mg(OH)<sub>2</sub> precursor (SiO<sub>2</sub>–MgO (III)<sub>nano</sub>), showing the highest degree of chemical contact between the SiO<sub>2</sub> and MgO components, gave the highest butadiene yield. Variation of the Mg/Si ratio in a series of SiO<sub>2</sub>–MgO (III)<sub>nano</sub> materials showed a volcano-type dependence of the butadiene yield on MgO content. <sup>1</sup>H–<sup>29</sup>Si CP-MAS NMR studies allowed for the identification of the type and an estimation of the amount of magnesium silicates formed during wet-kneading. Here, we argue that the structural characteristics of the hydrous magnesium silicates, lizardite and talc, formed during catalyst preparation, together with the ratio of the magnesium silicates to MgO, determine the overall acid/base properties of the SiO<sub>2</sub>–MgO (III)<sub>nano</sub> catalyst materials and as a result, catalyst performance.

**KEYWORDS:** ethanol-to-butadiene, wet-kneading, silica-magnesia, magnesium silicates, <sup>29</sup>Si NMR



## 1. INTRODUCTION

1,3-Butadiene (butadiene) is an important bulk chemical and finds its main application in the polymer industry, in particular in the synthesis of polybutadiene (PB) and acrylonitrile–butadiene–styrene (ABS) rubber. Currently, most of the butadiene is produced as a byproduct of the hydrocarbon steam cracking processes, although shifts to lighter feedstocks such as ethane (mainly recovered from shale gas deposits) may impact butadiene production.<sup>1</sup>

Given the recent increase in availability of bioethanol, the Lebedev process, in which ethanol is converted into butadiene, could provide a particularly attractive alternative. Recently, various types of metal-promoted catalysts have been reported for this process, including Ag/ZrO<sub>2</sub>/SiO<sub>2</sub>,<sup>2</sup> Hf–Zn/SiO<sub>2</sub>,<sup>3</sup> and ZrBEA zeolite<sup>4</sup> catalysts. SiO<sub>2</sub>–MgO-based systems have received much attention and typically perform well in terms of butadiene production.<sup>5,6</sup> The preparation method of these SiO<sub>2</sub>–MgO materials has been shown to be of pivotal importance for catalytic performance.<sup>7–9</sup> In particular, catalyst preparation by a technique known as wet-kneading gives SiO<sub>2</sub>–MgO materials that perform best. The term “wet-kneading”,

coined by Natta et al.,<sup>7</sup> is known to be a source of confusion and is therefore explicitly defined here as a process in which two or more solid precursor materials are combined and stirred (mechanically or magnetically) thoroughly in a liquid medium. To our best knowledge, Natta et al. were the first to use this method to prepare a SiO<sub>2</sub>–MgO catalyst from magnesium hydroxide and colloidal silica,<sup>7</sup> with the method now being commonly employed for the preparation of SiO<sub>2</sub>–MgO catalysts for the ethanol-to-butadiene process.<sup>10–13</sup>

Kvisle et al. showed that a physical mixture of SiO<sub>2</sub> and MgO performed worse than a wet-kneaded catalyst, highlighting the synergistic effect that is achieved upon mixing the two components with this preparation method.<sup>9</sup> We also previously showed wet-kneaded materials to perform much better than the physical mixture or materials prepared by coprecipitation.<sup>10</sup> On the contrary, Makshina and co-workers observed butadiene yield to vary only slightly for SiO<sub>2</sub>–MgO materials prepared by

Received: December 29, 2015

Revised: April 8, 2016

Published: May 26, 2016

mechanical dry mixing, wet-kneading or by excess solvent impregnation of  $\text{Mg}(\text{NO}_3)_2$  on  $\text{SiO}_2$ .<sup>14</sup> Not only the preparation method itself, but also choices made within a given preparation method can affect the performance of  $\text{SiO}_2$ – $\text{MgO}$  catalysts for the Lebedev process. Little variation has been reported, however, in terms of choice of Mg precursor. While some have used  $\text{MgO}$  as precursor to the hydroxide that is then formed in situ upon wet-kneading in water, more often  $\text{Mg}(\text{OH})_2$  is used directly in the wet-kneading step. For the latter, a commercial  $\text{Mg}(\text{OH})_2$  source has been used,<sup>15</sup> but more often the hydroxide is prepared fresh by precipitation from  $\text{Mg}(\text{NO}_3)_2$ .<sup>8,9,14</sup> Ohnishi et al. observed that a wet-kneaded catalyst made with  $\text{MgCl}_2$  as precursor to  $\text{Mg}(\text{OH})_2$  performed worse than one made from  $\text{Mg}(\text{NO}_3)_2$  as a result of some remaining traces of chloride.<sup>8</sup> Finally, Lewandowski et al. used a  $\text{MgO}$  that was prepared by calcination of  $(\text{MgCO}_3)_4 \cdot \text{Mg}(\text{OH})_2 \cdot 5\text{H}_2\text{O}$ ,<sup>16</sup> but they made no comparison with other  $\text{MgO}$  precursors.

Natta and Rigamonti noted the influence of the choice of kneading liquid, with catalysts prepared by kneading in water performing better than those prepared in ethanol.<sup>7</sup> Other examples of solvent effects are discussed below. The ratio between  $\text{SiO}_2$  and  $\text{MgO}$  is also known to strongly influence catalyst performance. For example, Niiyama et al. found a  $\text{SiO}_2$ – $\text{MgO}$  catalyst with a  $\text{MgO}$  content of 0.85 (see Experimental section for definition) to perform better than all other ratios tested, attributing this result to improved acid–base properties.<sup>15</sup> On the other hand, Ohnishi and co-workers observed the best catalytic performance for a sample having a 0.50  $\text{MgO}$  content.<sup>8</sup> Finally, Makshina et al. tested different ratios of the physically mixed components and found a 0.66  $\text{MgO}$  content to be best.<sup>14</sup> These different results suggest that a direct correlation between the ratio of the components and performance cannot be drawn unless other parameters (e.g., preparation details and structural properties) of the catalysts are taken into account.

Important questions still remain unanswered regarding the structural and chemical transformations that bring about the synergy shown by wet-kneaded  $\text{SiO}_2$ – $\text{MgO}$  catalysts. Natta and Rigamonti already provided some important insights in their early work, noting magnesium silicate formation by powder X-ray diffraction (XRD) for the water-kneaded samples, but not for the ones prepared in ethanol.<sup>7</sup> Interestingly, the extent of silicate formation correlated with butadiene production, with both limited and excessive amounts of silicates being detrimental for catalysis. Relatedly, Kvisle et al. noted that  $\text{Mg}$ – $\text{O}$ – $\text{Si}$  bonds are formed during wet-kneading of  $\text{SiO}_2$  and  $\text{Mg}(\text{OH})_2$ , based on a UV–vis band at  $\sim 260$  nm, a spectroscopic signature that is also observed for antigorite (a magnesium silicate of the serpentine group).<sup>9</sup> Based on  $^{29}\text{Si}$  magic angle spinning nuclear magnetic resonance (MAS NMR) and infrared spectroscopy (FT-IR) data, Janssens et al. recently also pointed at the formation of an amorphous magnesium silicate upon impregnation of dry milled  $\text{SiO}_2$ – $\text{MgO}$  materials with an aqueous Ag salt solution.<sup>13</sup> Although their formation and possible role in catalysis has thus been recognized, only a very limited number of studies actually purposefully used magnesium silicates as catalysts or as catalyst support for the Lebedev process. In one such rare example, Kitayama et al. observed that sepiolite (a magnesium silicate clay mineral) produced mainly ethylene and only trace amounts of butadiene.<sup>17</sup> Nonetheless, remarkable butadiene yields could be achieved upon addition of transition metals to the sepiolite

clay, a result attributed to increased dehydrogenation activity. A similar observation was made by Gruver and co-workers for Ag-promoted aluminated sepiolites.<sup>18</sup>

To better understand the relation between synthesis, structure and performance of wet-kneaded  $\text{SiO}_2$ – $\text{MgO}$  catalysts, we previously investigated the morphology, acidity–basicity and other physicochemical properties of a set of differently prepared materials (including via wet-kneading) and related these properties with their performance.<sup>10,11</sup> The wet-kneaded materials in particular showed significantly higher butadiene yields as a result of an intermediate amount of acid sites and a limited amount of strong basic ones. How the choice of preparation parameters affects structure and performance of wet-kneaded  $\text{SiO}_2$ – $\text{MgO}$  catalysts is largely unknown; it is nonetheless expected that variation of such parameters allows control over morphology, acid–base properties of the materials and, importantly, the amount and nature of the magnesium silicates that are formed during wet-kneading. The aim of this paper is therefore to rationalize the relation between the structure of the wet-kneaded catalysts and performance as a function of preparation method. Here, we show that variation of the Mg precursor and of  $\text{MgO}$  content determines the extent of magnesium silicates formation during wet-kneading, as well as their chemical nature. The formation of specific magnesium silicates is considered essential for efficient catalyst performance in the Lebedev ethanol-to-butadiene conversion.

## 2. EXPERIMENTAL SECTION

**2.1. Materials.** Tetraethyl orthosilicate (TEOS, 98%, Aldrich),  $\text{NH}_3$  (25%, Merck), ethanol (100%, Interchem),  $\text{Mg}(\text{NO}_3)_2 \cdot 6\text{H}_2\text{O}$  (99+%, Acros),  $\text{NaOH}$  (pellets for analysis, Merck),  $\text{Mg}(\text{OH})_2$  (reagent grade, 95%, Sigma-Aldrich), and  $\text{MgCO}_3$  (for biochemistry, specified according to the requirements of USP, Acros Organics) were all used as received without further purification.

**2.2. Catalyst Preparation.**  $\text{SiO}_2$ – $\text{MgO}$  (III) was synthesized according to a published procedure,<sup>10</sup> briefly summarized here: 1. The dried Stöber  $\text{SiO}_2$  component is prepared from TEOS in an ethanol/ $\text{NH}_3$  solution; after allowing the solution to age for 15 h, the solid obtained is dried for 1 h in a rotary evaporator; 2.  $\text{Mg}(\text{OH})_2$  is precipitated from the corresponding nitrate by addition of a 1 M aqueous  $\text{NH}_3$  solution and, afterward, dried at 393 K overnight; 3. The two components are then wet-kneaded in  $\text{H}_2\text{O}$  at RT for 4 h; finally, the resulting solid is dried at 393 K overnight and calcined for 5 h at 773 K.

For all catalysts used in this study, the preparation of the  $\text{SiO}_2$  component is identical to the one employed for  $\text{SiO}_2$ – $\text{MgO}$  (III) (described above). Three more samples were prepared using a different  $\text{MgO}$  precursor. For  $\text{SiO}_2$ – $\text{MgO}$  (III)<sub>nano</sub>,  $\text{Mg}(\text{OH})_2$  was precipitated from  $\text{Mg}(\text{NO}_3)_2$  using  $\text{NaOH}$  according to the procedure reported by Vatsha et al.<sup>19</sup> The desired amount of a 0.4 M  $\text{NaOH}$  aqueous solution was added dropwise to 250 mL of 0.2 M  $\text{Mg}(\text{NO}_3)_2$  in water, until the pH reached 12. This pH was maintained for 1 h, after which the solid was recovered by centrifugation and washed multiple times with deionized water.  $\text{SiO}_2$ – $\text{MgO}$  (III)<sub>nano</sub> was free of traces of sodium, as confirmed by inductively coupled plasma (ICP) analysis. For the  $\text{SiO}_2$ – $\text{MgO}$  (III)<sub>comm</sub> and  $\text{SiO}_2$ – $\text{MgO}$  (III)<sub>carb</sub> samples, the desired amount of commercially available  $\text{Mg}(\text{OH})_2$  and  $\text{MgCO}_3$ , respectively, were used as received in the standard wet-kneading procedure. For all catalysts, wet-kneading consisted of mixing the Mg and Si components at



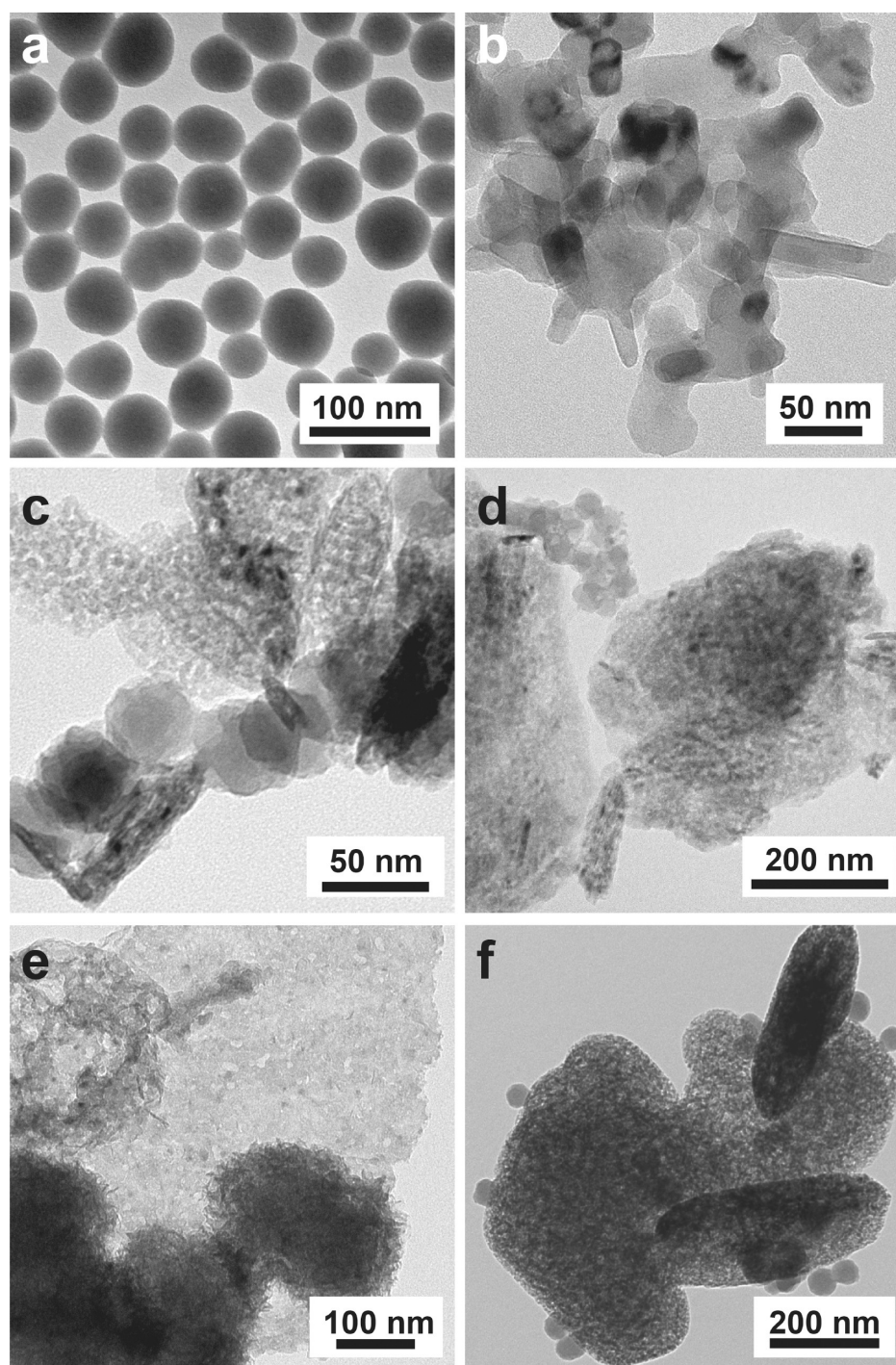


**Figure 1.** TEM images of the catalysts prepared using different Mg precursors. (a)  $\text{SiO}_2$ , (b)  $\text{MgO}_{\text{nano}}$ , (c)  $\text{SiO}_2\text{--MgO (III)}_{\text{nano}}$ , (d)  $\text{SiO}_2\text{--MgO (III)}$ , (e)  $\text{SiO}_2\text{--MgO (III)}_{\text{carb}}$ , and (f)  $\text{SiO}_2\text{--MgO (III)}_{\text{comm}}$ .

room temperature for 4 h in 200 mL of water (ratio  $\text{H}_2\text{O}/\text{solid} = 95.7$  (g/g)). All precipitates were washed several times with deionized water and recovered via centrifugation, dried at 393 K, and then calcined at 773 K for 5 h. All catalysts prepared as described above have a MgO content (defined as  $\text{mol}_{\text{MgO}}/(\text{mol}_{\text{MgO}} + \text{mol}_{\text{SiO}_2})$ ) of 0.50. Furthermore, for  $\text{SiO}_2\text{--MgO (III)}_{\text{nano}}$ , four more samples with MgO contents 0.33, 0.60, 0.66, and 0.75 were prepared by using the required amounts of  $\text{Mg}(\text{OH})_2$  and  $\text{SiO}_2$  during wet-kneading. After wet-kneading,  $\text{SiO}_2\text{--MgO (III)}_{\text{nano}}$  catalysts were again dried overnight at 393 K and calcined at 773 K for 5 h.

**2.3. Catalyst Characterization.** Transmission electron microscopy (TEM) images of the various samples were obtained on a Tecnai 12 apparatus, operated at 120 keV. The catalyst particles were sonicated in ethanol and deposited on a Cu TEM grid prior to analysis. STEM-EDX analyses were performed with a Tecnai F20 apparatus, operating at 200 keV and equipped with an energy-dispersive X-ray (EDX) detector.

A Tecnai FEI XL 30SFEG scanning electron microscope (SEM) was used to compare the size and morphology of  $\text{Mg}(\text{OH})_2$  particles used to prepare  $\text{SiO}_2\text{--MgO (III)}$  and  $\text{SiO}_2\text{--MgO (III)}_{\text{nano}}$ .

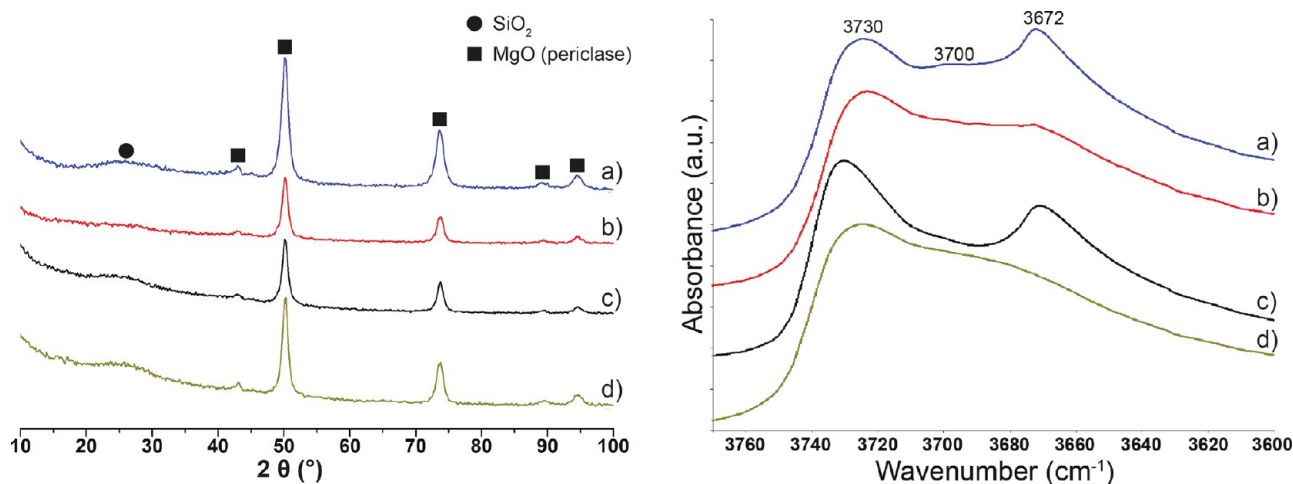


**Figure 2.** (left) XRD patterns of (a) SiO<sub>2</sub>-MgO (III)<sub>nano</sub>, (b) SiO<sub>2</sub>-MgO (III), (c) SiO<sub>2</sub>-MgO (III)<sub>carb</sub>, and (d) SiO<sub>2</sub>-MgO (III)<sub>comm</sub> in the range 10–100 2θ degree and (right) FT-IR spectra of the catalysts prepared using different Mg precursors. The spectra, recorded at 823 K, are offset for clarity.

X-ray powder diffraction (XRD) patterns were obtained by a Bruker-AXS D2 Phaser powder X-ray diffractometer using Co Kα<sub>1,2</sub> with λ = 1.79026 Å, operated at 30 kV. Measurements were carried out in the range of 10–100 2θ degrees using a step size of 0.15 2θ degrees and a scan speed of 0.5 s.

Fourier transform infrared spectroscopy (FT-IR) measurements were taken with 25 scans per spectrum on a PerkinElmer System 2000 with a DTGS detector and a resolution of 4 cm<sup>-1</sup>. Approximately 15 mg of the catalyst were pressed into a pellet and placed into the infrared cell. The catalyst was dried in the cell under vacuum with a temperature ramp of 5 K min<sup>-1</sup> reaching the desired temperature of 823 K; FT-IR spectra were taken every 25 K in the temperature range 323–823 K. Once 823 K was reached, this temperature was kept constant for 30 min; spectra were taken at 5, 10, and 30 min after reaching the maximum temperature.

Solid-state nuclear magnetic resonance (NMR) experiments were recorded on a Bruker spectrometer operating at a <sup>1</sup>H Larmor frequency of 500 MHz, equipped with a 3.2 mm magic angle spinning (MAS) probe, using a 12 kHz MAS frequency and at a temperature of 298 K. After a 94 kHz <sup>1</sup>H excitation pulse, Hartmann–Hahn <sup>1</sup>H–<sup>29</sup>Si cross-polarization (CP) was achieved using a 58 kHz <sup>1</sup>H field with a 70–100% ramp, a 71 kHz <sup>29</sup>Si field, and a contact time of 8 ms. During acquisition 31 kHz SPINAL64,<sup>20</sup> <sup>1</sup>H decoupling was applied, and a 4 s interscan delay was used.<sup>20</sup> Proton detected 2D <sup>29</sup>Si–<sup>1</sup>H spectra were recorded with a long <sup>1</sup>H–<sup>29</sup>Si CP (8 ms) followed by a shorter <sup>29</sup>Si–<sup>1</sup>H CP (2.5 ms) after the <sup>29</sup>Si t1 period to ensure polarization transfer only to the closest protons (Figure S1).<sup>21</sup> Prior to the last CP, a 6 kHz MISSISSIPPI<sup>22</sup> block (τ = 5 ms, N = 4) ensures destruction of on-resonance bulk proton magnetization. 1D spectra were processed using 50 Hz line-broadening; for the 2D, linear prediction was used to double the points in the indirect dimension and a 0.25π shifted squared sine bell window was applied to both time dimensions. All spectra were referenced to tetramethylsilane (TMS). The spectra were deconvoluted using MestReNova software (ver. 10.0.2), assuming a Gaussian distribution for each deconvoluted chemical shift distribution.

**2.4. Catalyst Testing.** The various catalysts were tested according to the procedure reported previously.<sup>10</sup> In particular, 0.2 g of catalyst was added into a quartz reactor. The desired

amount of ethanol was fed via a Bronkhorst CEM (controlled evaporation mixing) system. The total flow used was 100 mL min<sup>-1</sup>, of which 2 mL min<sup>-1</sup> consisted of ethanol (in the gas phase), with the remainder being nitrogen. Reactions were run at 698 K and an WHSV of 1.1 h<sup>-1</sup>.

In all cases, the analysis of the reaction mixture was performed via online GC-FID; quantification of the main components (i.e., ethanol, ethylene, acetaldehyde, and butadiene) was based on calibration curves obtained by feeding known amounts of the various compounds. The following definitions were used (mol: moles of observed substance):

Ethanol conversion:

$$X_{\text{EtOH}}(\%) = 100 \times \frac{\text{mol}_{\text{EtOH converted}}}{\text{mol}_{\text{EtOH initial}}}$$

Yields (acetaldehyde, ethylene):

$$Y_i(\%) = 100 \times \frac{\text{mol}_{\text{product } i}}{\text{mol}_{\text{EtOH converted}}}$$

Yields (butadiene):

$$Y_i(\%) = 100 \times 2 \times \frac{\text{mol}_{\text{product } i}}{\text{mol}_{\text{EtOH converted}}}$$

Selectivity of the i-main component:

$$S_i(\%) = 100 \times \frac{Y_i}{X_{\text{EtOH}}}$$

### 3. RESULTS AND DISCUSSION

#### 3.1. Influence of Mg Precursors on Performance.

Previously, we showed silica particle size to have a remarkable effect on the catalytic performance of wet-kneaded SiO<sub>2</sub>-MgO materials, with SiO<sub>2</sub>-MgO (III), prepared using silica spheres of 30–100 nm in diameter, performing best.<sup>10</sup> To study the influence of MgO structure and particle size on ethanol-to-butadiene catalysis as a function of Mg precursor, three more catalysts were synthesized and compared with the benchmark SiO<sub>2</sub>-MgO (III) catalyst. SiO<sub>2</sub>-MgO (III)<sub>nano</sub> was synthesized by precipitation of Mg(OH)<sub>2</sub> from Mg(NO<sub>3</sub>)<sub>2</sub> following the procedure reported by Vatsha et al.,<sup>19</sup> to assess the effect of the



significantly smaller  $\text{Mg}(\text{OH})_2$  particle size on wet-kneading efficiency and catalyst structure (Figure S2).  $\text{SiO}_2\text{--MgO}$  (III)<sub>comm</sub> was prepared from a commercial  $\text{Mg}(\text{OH})_2$  source and  $\text{SiO}_2\text{--MgO}$  (III)<sub>carb</sub>, finally, was prepared with commercial  $\text{MgCO}_3$  (chosen because of the significant amount of carbonates that can be present as adsorbates on  $\text{MgO}$ ).<sup>11</sup>

TEM images of the catalysts prepared with different  $\text{MgO}$  precursors show significant morphological differences (Figure 1). In  $\text{SiO}_2\text{--MgO}$  (III),  $\text{SiO}_2$ -rich areas are formed by aggregation of the  $\text{SiO}_2$  spheres together with relatively large  $\text{MgO}$ -like sheets. A significant degree of interaction was also noted as the  $\text{SiO}_2$  spheres and  $\text{MgO}$  sheets are in close contact with each other. Moreover, the  $\text{SiO}_2$ -like and  $\text{MgO}$ -like areas in  $\text{SiO}_2\text{--MgO}$  (III) have a significantly rougher morphology compared to the individual components.

This suggests that considerable morphological and possibly chemical changes occur during wet-kneading. The morphology of  $\text{SiO}_2\text{--MgO}$  (III)<sub>nano</sub>, prepared with a  $\text{Mg}(\text{OH})_2$  source of significantly smaller particle size (Figure S2), is quite similar to the benchmark catalyst, with the important exception that the  $\text{MgO}$  sheets are now indeed also much smaller than in the latter, and as a result, more intimate contact between the individual components is achieved. For  $\text{SiO}_2\text{--MgO}$  (III)<sub>comm</sub>, the use of commercial  $\text{Mg}(\text{OH})_2$  resulted in extremely regular  $\text{MgO}$  sheets. This seems to have significantly hindered the chemical interaction between the  $\text{SiO}_2$  and  $\text{Mg}(\text{OH})_2$  components during wet-kneading, as can be seen from the limited contact between the phases in the TEM image. Finally, the morphology of  $\text{SiO}_2\text{--MgO}$  (III)<sub>carb</sub> is quite dissimilar from the other samples.  $\text{SiO}_2$  spheres can be hardly recognized and they seem to be more dispersed into the  $\text{MgO}$  component; the  $\text{MgO}$  sheets, on the other hand, show a less corrugated structure. The XRD patterns of the catalysts are dominated by the  $\text{MgO}$  periclase peaks (Figure 2); a halo can furthermore be seen in the region  $20\text{--}30^\circ 2\theta$  due to amorphous silica. The order of crystallinity, as demonstrated by the intensity of the periclase reflections, of  $\text{SiO}_2\text{--MgO}$  (III)<sub>nano</sub> >  $\text{SiO}_2\text{--MgO}$  (III)<sub>comm</sub>  $\gg$   $\text{SiO}_2\text{--MgO}$  (III)<sub>carb</sub> >  $\text{SiO}_2\text{--MgO}$  (III) does not correlate with catalytic performance (see below). The high crystallinity of  $\text{SiO}_2\text{--MgO}$  (III)<sub>comm</sub> is in line with the structure seen by TEM. For all catalysts, no other reflections (e.g., ones arising from magnesium silicates) could be observed. Interestingly, Natta et al. observed reflections of nonidentified magnesium silicates only if their materials had been calcined at 973 K (i.e., a temperature significantly higher than the calcination temperature of 773 K employed here).<sup>7</sup> The magnesium silicates that are formed to different extents on the  $\text{SiO}_2\text{--MgO}$  materials after wet-kneading and calcination (see below) thus do not show any long-range order.

FT-IR spectroscopy provided valuable information on the types of OH groups present on the wet-kneaded  $\text{SiO}_2\text{--MgO}$  catalysts, in particular on those associated with the magnesium silicates.<sup>11</sup> The wet-kneaded  $\text{SiO}_2\text{--MgO}$  samples show three broad OH vibrations at  $\sim 3730$ ,  $\sim 3700$ , and  $\sim 3672\text{ cm}^{-1}$  (Figure 2); the spectra of the individual Stöber  $\text{SiO}_2$  and  $\text{MgO}_{\text{nano}}$  components, both calcined at 773 K for 5 h, are shown in Figure S3. For  $\text{SiO}_2$ , the broad SiOH band at  $3725\text{ cm}^{-1}$  is the result of the several types of silanols present,<sup>23</sup> while the MgOH stretching vibration at  $3735\text{ cm}^{-1}$  seen for  $\text{MgO}_{\text{nano}}$  is accompanied by a broad shoulder between 3700 and  $3400\text{ cm}^{-1}$ , attributed to multicoordinated surface OH groups.<sup>24</sup> Based on these features, the band observed for the  $\text{SiO}_2\text{--MgO}$  samples at  $\sim 3730\text{ cm}^{-1}$  is thought to arise from contributions

of both SiOH and MgOH groups; magnesium silicates formed during wet-kneading might also contribute to this band, as indicated by low-temperature FTIR experiments after CO adsorption (data not shown). Most notably, the two new features at around  $3700$  and  $3670\text{ cm}^{-1}$  are here attributed to magnesium silicates formation, with the  $\text{SiO}_2\text{--MgO}$  (III)<sub>nano</sub> catalyst showing the highest intensity of these magnesium silicates vibrations. Indeed, we noted previously that only samples prepared by wet-kneading showed a peak at  $\sim 3672\text{ cm}^{-1}$ .<sup>11</sup> Relatedly, Janssens et al.<sup>13</sup> also reported on similar OH bands thought to originate from different magnesium silicates. A more detailed assignment of the bands to specific magnesium silicates is precluded, however, by the fact that the FT-IR features reported for various magnesium silicates are all rather similar (e.g.,  $3670\text{ cm}^{-1}$  for antigorite,<sup>25</sup>  $3674\text{ cm}^{-1}$  for talc,<sup>26</sup>  $3680\text{ cm}^{-1}$  for lizardite,<sup>27</sup> etc.).

Little is actually known of the extent to which magnesium silicates are formed, of their nature, and of how they influence the catalytic properties of the wet-kneaded  $\text{SiO}_2\text{--MgO}$  catalysts. Quantification of the magnesium silicates could thus be useful, as this is expected to correlate with catalyst performance, as previously suggested.<sup>7</sup> It can indeed be seen in Figure 2 that the extent of magnesium silicate formation varies with  $\text{MgO}$  precursor. However, the large number of different OH groups present on the two single oxides and the unknown nature of the magnesium silicates, precluded a scientifically meaningful deconvolution of the spectra in the  $3770\text{--}3600\text{ cm}^{-1}$  region and thus quantification based on the FT-IR spectra alone. As shown below for a second set of samples, solid-state  $^{29}\text{Si}$  NMR measurements can provide more detailed information on the type and extent of magnesium silicate formation, however.

The mechanism by which magnesium silicates form during wet-kneading has hardly been studied.  $\text{Mg}(\text{OH})_2$  is slightly soluble in  $\text{H}_2\text{O}$ , leading to the formation of  $[\text{Mg}(\text{H}_2\text{O})_6]^{2+}$  cations in solution<sup>28</sup> and causing the aqueous medium of a typical wet-kneading synthesis to be alkaline. For example, the wet-kneading suspension used for  $\text{SiO}_2\text{--MgO}$  (III)<sub>nano</sub> had a pH of approximately 9.0–10.0 (see Figure S4), with similar pH ranges being noted for the wet-kneading suspensions of the other catalysts. Under such alkaline conditions, the surface species of the  $\text{SiO}_2$  component will, in turn, also partially dissolve and form reactive, soluble  $[\text{SiO}_2(\text{OH})_2]^{2-}$  silicate anions.<sup>29</sup> Given the opposite surface charges of the solid  $\text{Mg}(\text{OH})_2$  and  $\text{SiO}_2$  precursors under wet-kneading conditions (isoelectronic point (IEP) of  $\text{Mg}(\text{OH})_2 > \text{pH } 12$  and  $\text{IEP}_{\text{SiO}_2} \approx \text{pH } 2$ ), the soluble Mg-containing cations are then expected to redeposit on the silica component and, conversely, the Si-containing anions on the magnesia component. This suggests that the surface of each component is thus decorated with a certain amount of the other one, allowing for the formation of Mg silicates on the outer surface of the catalysts.

In fact,  $\text{Mg}(\text{OH})_2$  is actually heavily used for industrial water system purification to bring about the removal of  $\text{SiO}_2$  via precipitation.<sup>30</sup> Li and co-workers furthermore showed that this dissolution/precipitation mechanism also governs the preparation of cementitious materials from  $\text{MgO}$  and silica fume in  $\text{H}_2\text{O}$ .<sup>31</sup> Indeed, they observed an initial increase in pH, due to partial solubilization of  $\text{Mg}(\text{OH})_2$ , thus causing  $\text{SiO}_2$  to partially dissolve; the formation of magnesium silicates then occurs together with a decrease in pH until a plateau is reached.

Such a mechanism of magnesium silicates formation involving dissolution and reprecipitation of the components,

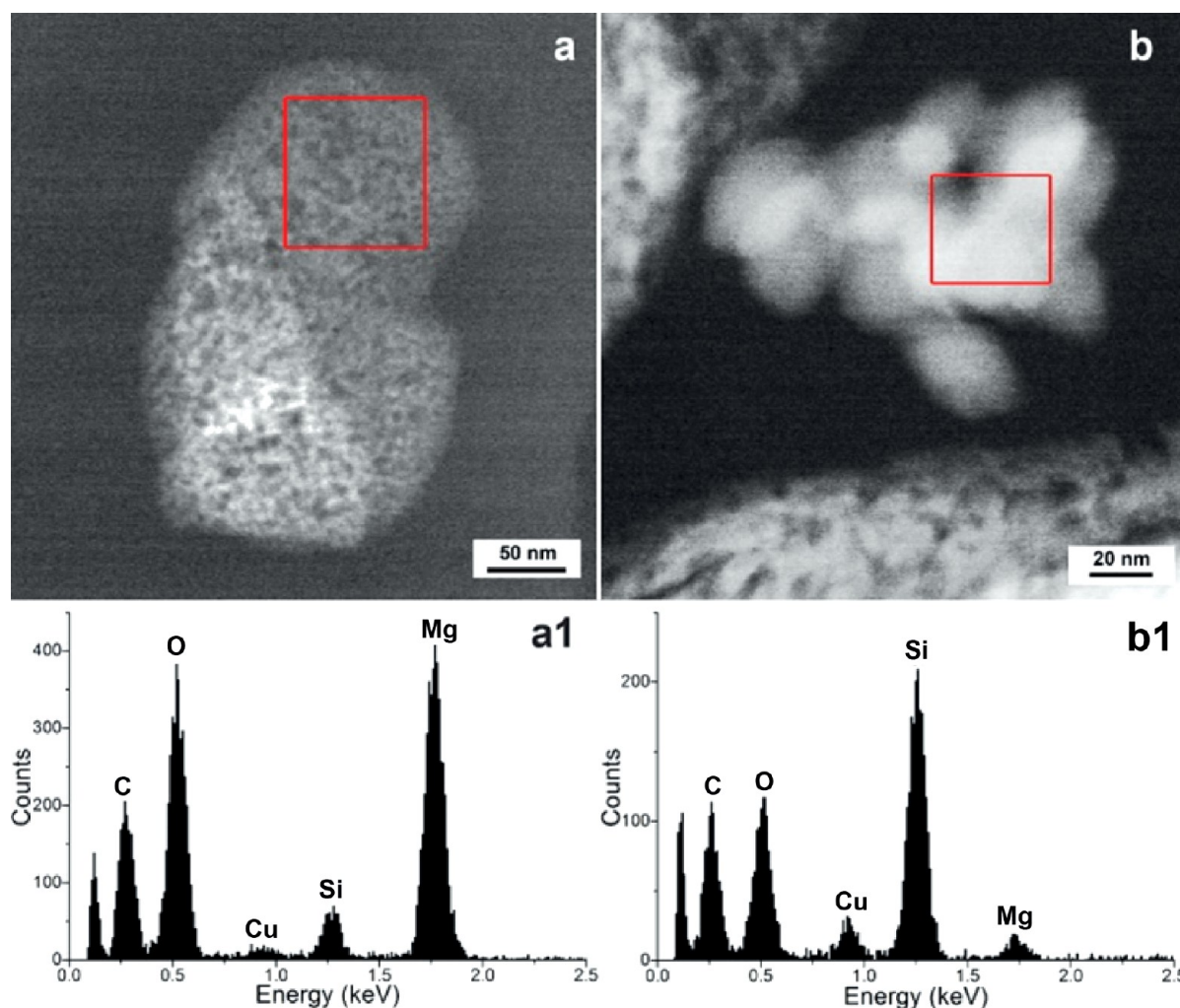


**Figure 3.** STEM-EDX analysis of (a) a particle having morphological features of MgO and (a1) corresponding EDX spectrum, (b) a particle having morphological features of SiO<sub>2</sub> and (b1) corresponding EDX spectrum.

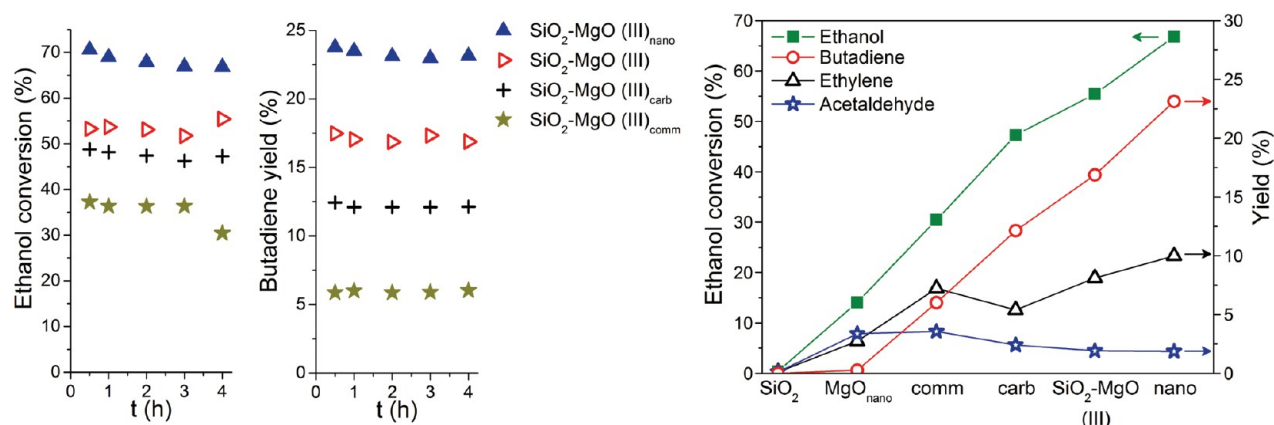


**Figure 4.** Comparison of the ethanol conversion (left), butadiene yield (center), and yield of the main products after 4 h time on stream (right) for four catalysts prepared with different MgO precursors (comm, carb, and nano refers to SiO<sub>2</sub>–MgO (III)<sub>comm</sub>, SiO<sub>2</sub>–MgO (III)<sub>carb</sub>, and SiO<sub>2</sub>–MgO (III)<sub>nano</sub> catalysts, respectively).

would explain the morphology changes observed for both the SiO<sub>2</sub> and MgO components upon wet-kneading, as evidenced by TEM (Figure 1). The Stöber SiO<sub>2</sub> spheres clearly show a more rough and irregular surface after wet-kneading; similarly, MgO (initially consisting of dense, regular sheets) shows a much more corrugated and rough structure after wet-kneading.

STEM-EDX analyses, as exemplified for SiO<sub>2</sub>–MgO (III) in Figure 3, confirmed the suggested cross-deposition. A region of the catalyst with sheet-like morphology typical of MgO particles indeed does contain a non-negligible amount of Si (depending on the specific particle, ~5–20 wt %). Similarly, Mg is found on SiO<sub>2</sub>-rich areas of the catalyst, albeit in a lower

amount, which is in line with the lower solubility of  $\text{Mg}(\text{OH})_2$ . This, together with the new features of FT-IR spectra and the change in morphology observed, again points at magnesium silicate formation.

The structural differences seen for the catalysts prepared with different MgO precursors are reflected in their remarkably different performance, as shown in Figure 4. In contrast with the wet-kneaded  $\text{SiO}_2\text{--MgO}$  (III) catalysts, pure  $\text{SiO}_2$  gave negligible ethanol conversion, whereas pure MgO gave a low but significant conversion (i.e.,  $\sim 15\%$ ), producing only trace amounts of butadiene. Notably,  $\text{SiO}_2\text{--MgO}$  (III)<sub>nano</sub> showed an increase in butadiene yield and selectivity (i.e.,  $\sim 35$  vs  $30\%$ ) as compared with the benchmark catalyst  $\text{SiO}_2\text{--MgO}$  (III).  $\text{SiO}_2\text{--MgO}$  (III)<sub>comm</sub>, on the other hand, shows the worst performance. Notably, the  $\text{SiO}_2\text{--MgO}$  (III)<sub>nano</sub> catalyst achieved a BD productivity of  $0.253 \text{ g}_{\text{BD}} \text{ g}_{\text{cat}}^{-1} \text{ h}^{-1}$ ; the catalyst can thus compete well with the recently reported metal-promoted catalysts, which show very similar productivities ( $0.237$  for  $1\text{Ag}/10\text{ZrO}_2/\text{SiO}_2$ ,<sup>2</sup>  $0.264$  for  $\text{Hf}_{2.5}\text{Zn}_{1.6}/\text{SiO}_2$ ,<sup>3</sup> and  $0.280 \text{ g}_{\text{BD}} \text{ g}_{\text{cat}}^{-1} \text{ h}^{-1}$  for ZrBEA zeolite<sup>4</sup>). The product distribution (Figure 4) shows that the catalyst that gives the best butadiene yield also produces the most ethylene. The amount of acetaldehyde, considered a key intermediate for butadiene production,<sup>9,15,32</sup> that is produced over  $\text{SiO}_2\text{--MgO}$  (III)<sub>nano</sub> and  $\text{SiO}_2\text{--MgO}$  (III) is similar. As the acetaldehyde yield observed is the amount formed minus the amount further converted,<sup>5</sup> the higher butadiene yield observed for  $\text{SiO}_2\text{--MgO}$  (III)<sub>nano</sub> then implies that aldol condensation is more efficient for this catalyst. The opposite is true for  $\text{SiO}_2\text{--MgO}$  (III)<sub>comm</sub>, which shows remarkably low ethanol conversion and butadiene yield, even though producing a higher amount of acetaldehyde. Catalyst performance thus correlates with the extent of chemical contact between the two components. Indeed, for all catalysts, the order of catalytic performance agrees with the chemical interaction between the two wet-kneaded components, as indicated by the TEM and FT-IR results. It should be noted that not only the nature of the MgO precursor will strongly influence the structural properties of the catalyst (and thus performance), but also the ratio of MgO to  $\text{SiO}_2$  used during catalyst preparation. This ratio will, among others, also influence the nature and amount of magnesium silicate phases formed. In fact, given that synthesized pure Stöber  $\text{SiO}_2$  is catalytically inert (see next section), it is proposed that the ratio and proximity of the MgO and magnesium silicates phases is most relevant for catalysis and that these can be in part controlled by adjusting the MgO content.

**3.2. Influence of MgO Content on Performance.** Very different MgO contents have been reported to give optimal performance for wet-kneaded catalysts, perhaps because different preparation parameters are used in the various studies. In addition to the examples listed above, Kitayama and co-workers provided a key example on the influence of MgO content and the role of silicate formation in their investigation of the performance of ternary oxides prepared with different amounts of  $\text{SiO}_2$  and MgO and a fixed content of  $\text{NiO}$ <sup>33</sup> and suggested that a layered nickel magnesium silicate was formed for those catalysts with a MgO content of  $0.20\text{--}0.40$ . Butadiene yields followed a volcano-shaped dependence with the sample with  $0.40$  MgO content giving the maximum yield; its superior butadiene yield was attributed to the presence of the nickel magnesium silicate phase together with a small quantity of free MgO. Building on these results and using the best catalyst of this investigation as a reference (i.e.,  $\text{SiO}_2\text{--MgO}$  (III)<sub>nano</sub>), the

effect of MgO content on the structure and performance of the  $\text{SiO}_2\text{--MgO}$  catalysts was studied, for which four more samples were synthesized with MgO contents of  $0.33$ ,  $0.60$ ,  $0.66$ , and  $0.75$ . For comparison, the pure oxides  $\text{SiO}_2$  and MgO were also tested (MgO content of  $0$  and  $1$ , respectively).

The FT-IR spectra of the  $\text{SiO}_2\text{--MgO}$  (III)<sub>nano</sub> materials with different MgO content show that the hydroxyl bands of the samples are almost unchanged in position, but do differ in width and intensity (Figure 5). For instance, the features

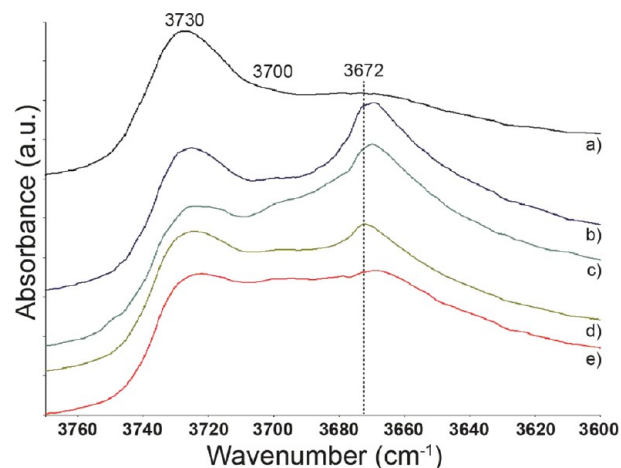


**Figure 5.** FT-IR spectra of the  $\text{SiO}_2\text{--MgO}$  (III)<sub>nano</sub> catalysts with different MgO content: (a)  $0.75$ , (b)  $0.66$ , (c)  $0.60$ , (d)  $0.50$ , and (e)  $0.33$ . The spectra, taken at  $823 \text{ K}$ , are offset for clarity.

attributed to magnesium silicates formation can be barely seen for the  $0.75$  sample, which is probably due to the amount of  $\text{SiO}_2$  being insufficient for significant silicate phase formation. On the other hand, the magnesium silicate band at  $\sim 3672 \text{ cm}^{-1}$  is significantly lower in intensity for the  $0.33$  sample than for the catalyst material with  $0.50$  MgO content. It should be noted, however, that the broad  $\text{SiO}_2$  and MgO features centered at  $\sim 3730 \text{ cm}^{-1}$  can also contribute to the intensity at the position of the magnesium silicate bands, urging some caution in the interpretation of its intensity. Nonetheless, it can be clearly seen that the band at  $\sim 3700 \text{ cm}^{-1}$  differs in intensity for samples with different MgO content; the magnesium silicate bands at  $\sim 3672 \text{ cm}^{-1}$  differ not only in intensity but also in shape (Figure 5). In particular, they are significantly broadened and seem to show two local maxima, suggesting the existence of additional magnesium silicate phase(s) having an OH stretch vibration at a slightly lower wavenumber (estimated at  $3669 \text{ cm}^{-1}$ ).

Previously, the nature of magnesium silicates has been studied with several characterization techniques including XRD,<sup>32,34</sup> Raman,<sup>35,36</sup> and NMR spectroscopy.<sup>37–40</sup> As for the precursor variation, no diffraction patterns of magnesium silicates were seen in the samples with different MgO content, suggesting that the magnesium silicates are amorphous or low in abundance and show only very weak diffraction, see Figure S5.<sup>41,42</sup> Raman spectroscopy also did not prove useful for our materials.  $^1\text{H}\text{--}^{29}\text{Si}$  CP-MAS NMR measurements did, however, provide additional information on the nature of the Mg silicates; the spectra of  $\text{SiO}_2$  and wet-kneaded  $\text{SiO}_2\text{--MgO}$  (III)<sub>nano</sub> samples with different MgO content are shown in Figure 6. It should be noted here that the signal intensities in these spectra depend not only on the molar ratios of the different species present in the samples but also on the  $^1\text{H}$



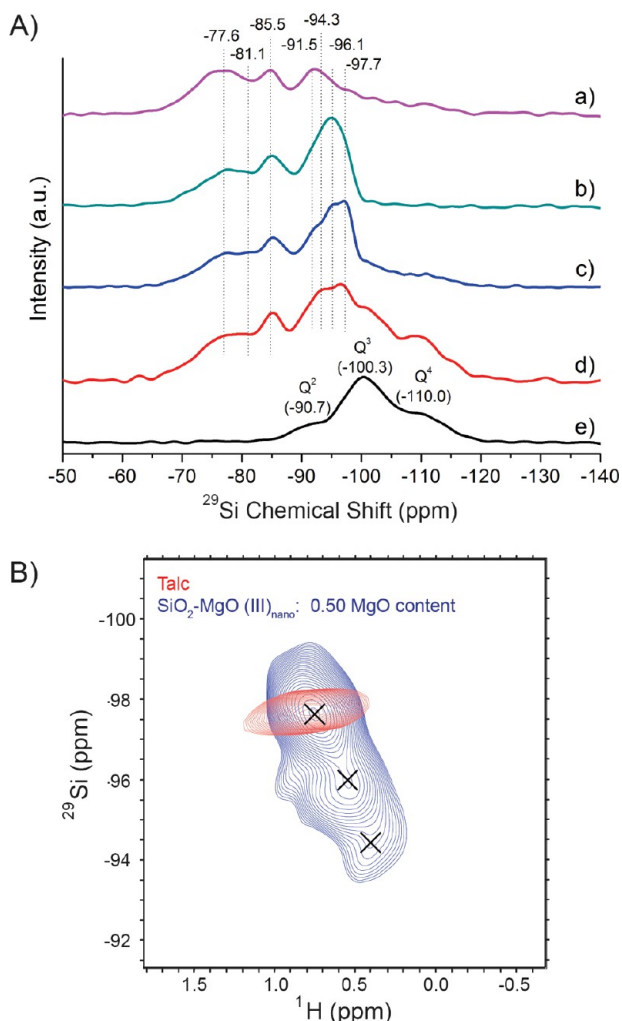


**Figure 6.** (A)  $^1\text{H}$ – $^{29}\text{Si}$  cross-polarized MAS NMR spectra of the  $\text{SiO}_2$ – $\text{MgO}$  (III) <sub>nano</sub> catalysts with different MgO content; (a) 0.75, (b) 0.66, (c) 0.50, (d) 0.33, and (e) 0 ( $\text{SiO}_2$ ). (B) 2D  $^1\text{H}$ – $^{29}\text{Si}$  CP-MAS  $^{29}\text{Si}$ – $^1\text{H}$  spectra of  $\text{SiO}_2$ – $\text{MgO}$  (III) <sub>nano</sub> with 0.50 MgO content (blue) and talc (purchased from Sigma-Aldrich; red). Crosses indicate signals from the three main species detected in this spectrum.

density around the  $^{29}\text{Si}$  nucleus and the  $^1\text{H}$ – $^{29}\text{Si}$  distance in those species; the shorter the distance and the higher the density, the more efficient the cross-polarization. In addition, differences in relaxation rates will also modulate the polarization transfer efficiency. The signals observed by CP-MAS NMR experiments are categorized into  $\text{Q}^n$  species ( $n$ , indicates the number of siloxane units around silicon), according to literature.<sup>43,44</sup> The synthesized  $\text{SiO}_2$  (calcined at 773 K for 5 h) shows three broad signals at  $-90.7$ ,  $-100.2$ , and  $-110.1$  ppm, which are attributed to geminal silanol ( $\text{Q}^2$ ,  $(\text{SiO})_2\text{Si}(\text{OH})_2$ ), simple silanol ( $\text{Q}^3$ ,  $(\text{SiO})_3\text{Si}(\text{OH})$ ), and siloxane groups ( $\text{Q}^4$ ,  $(\text{SiO})_4\text{Si}$ ).<sup>45</sup> Although the  $\text{Q}^4$  species must be more abundant, this is not reflected in the signal intensity, due to inefficient cross-polarization transfer from protons near the  $\text{Q}^4$  species at the applied contact time of 8 ms.<sup>46,47</sup> The  $\text{Q}^2$ ,  $\text{Q}^3$ , and  $\text{Q}^4$  signals can also be seen in the wet-kneaded samples, indicating the presence of unreacted  $\text{SiO}_2$ , especially for the samples with lower MgO content.

Notably, for the MgO-containing samples, the peaks are shifted downfield significantly, and the spectra are dramatically different from  $\text{SiO}_2$ . Given the extensive overlap, the CP-MAS

NMR spectra were deconvoluted and results are summarized in Figure 7 and Table S1. Seven additional signals are observed, centered at  $-77.6$ ,  $-81.1$ ,  $-85.5$ ,  $-91.5$ ,  $-94.3$ ,  $-96.1$ , and  $-97.8$  ppm, which vary in relative intensity for the different samples. This clearly suggests that the chemical environment near silicon has been altered by the wet-kneading process. Concomitantly, the ratio between (all) magnesium silicates and the retained silicon species tends to increase with MgO content, implying that the dissolved Si species do indeed reprecipitate as magnesium silicates. Furthermore, the decrease in  $\text{Q}^2/\text{Q}^4$  ratio from 0.43 for  $\text{SiO}_2$  to 0.3 or less for the wet-kneaded samples, shows that, expectedly, the  $\text{Q}^2$  surface silanol groups (as well as the simple ones) are more reactive than the siloxane groups for the formation of magnesium silicates during wet-kneading.

Because the wet-kneading of dried Stöber  $\text{SiO}_2$  and  $\text{Mg}(\text{OH})_2$  is performed in water, hydrous magnesium silicates are thought to be formed first. After that, anhydrous magnesium silicates such as forsterite ( $\text{Mg}_2\text{SiO}_4$ ) and enstatite ( $\text{MgSiO}_3$ ) are expected to be formed by thermal decomposition during the subsequent calcination step.<sup>28</sup> Based on Chen et al., the signal seen at around  $-77.6$  ppm can be assigned to a Mg silicate phase intermediate between forsterite and enstatite.<sup>42</sup> They observed signals at  $-77.6$ ,  $-84.8$ , and  $-91.8$  ppm for magnesia-silica mixtures prepared by mechanical grinding, attributing the first peak to an amorphous dehydroxylated intermediate phase between the  $\text{Q}^0$  and  $\text{Q}^2$  species of forsterite and enstatite (which would appear around  $-62$  ppm and  $-83$  ppm, respectively).<sup>37,48</sup> For this amorphous dehydroxylated intermediate phase in the  $\text{SiO}_2$ – $\text{MgO}$  (III) <sub>nano</sub> catalysts, the peak position gradually shifts downfield from  $-78.0$  to  $-77.0$  ppm, and the area percentage increases with MgO content. This downfield shift suggests that relatively more forsterite is present in the samples with a higher MgO content, in line with the difference in Mg to Si ratio in enstatite (1:1) and forsterite (2:1). The alternative assignment of the signal at  $-77.6$  ppm to  $\text{Q}^2$  structures in  $\text{Na}_2\text{SiO}_3$  ( $-76.8$  ppm)<sup>36</sup> is discarded, as ICP analysis confirmed the samples to be free of traces of sodium, even though sodium hydroxide was used as precipitant in the preparation of the Mg precursor. The very small signal at  $-81.1$  ppm seen for some of the samples can be assigned to ringwoodite ( $\gamma\text{-Mg}_2\text{SiO}_4$ ,  $-81.3$  ppm),<sup>49</sup> a spinel-type olivine polymorph of forsterite ( $\alpha\text{-Mg}_2\text{SiO}_4$ ).<sup>50</sup>

As the TEM and FT-IR data suggested a correlation between the intensity/position of hydroxyl groups of the magnesium silicates and catalytic activity, we here also focus on those NMR signals belonging to hydrous magnesium silicates (i.e., those in the region of  $-85$  to  $-98$  ppm).<sup>43</sup> Similar to the first two signals seen in our data in that region at  $-85.5$  and  $-91.5$  ppm, magnesia-silica materials prepared by mechanochemical pot milling of brucite and silicic acid showed signals at  $-84.3$  and  $-91.5$  ppm;<sup>38</sup> furthermore, for a sample prepared by wet-impregnation of a commercial silica with  $\text{Mg}(\text{NO}_3)_2$ , peaks were detected at  $-84$  and  $-92.5$  ppm and assigned to  $\text{Q}^2(\text{Mg},\text{OH})$  and  $\text{Q}^3(\text{Mg})$  units of a structurally ill-defined (amorphous) hydrous silicate.<sup>51</sup> Similarly, the two signals at  $-85.5$  and  $-91.5$  ppm do not show a cross-peak in the 2D proton-detected  $^{29}\text{Si}$ – $^1\text{H}$  CP-MAS NMR spectrum, indicating the absence of structural and well-ordered OH groups (Figure 6 and Figure S1).<sup>52</sup> Such peaks at  $-85$  and  $-92$  ppm were also observed for dry milled  $\text{SiO}_2$ – $\text{MgO}$  materials with an aqueous Ag salt solution<sup>13</sup> and again assigned to  $\text{Si}(\text{OMg})(\text{OSi})_2(\text{OH})$  and  $\text{Si}(\text{OMg})(\text{OSi})_3$  species, respectively. An alternative



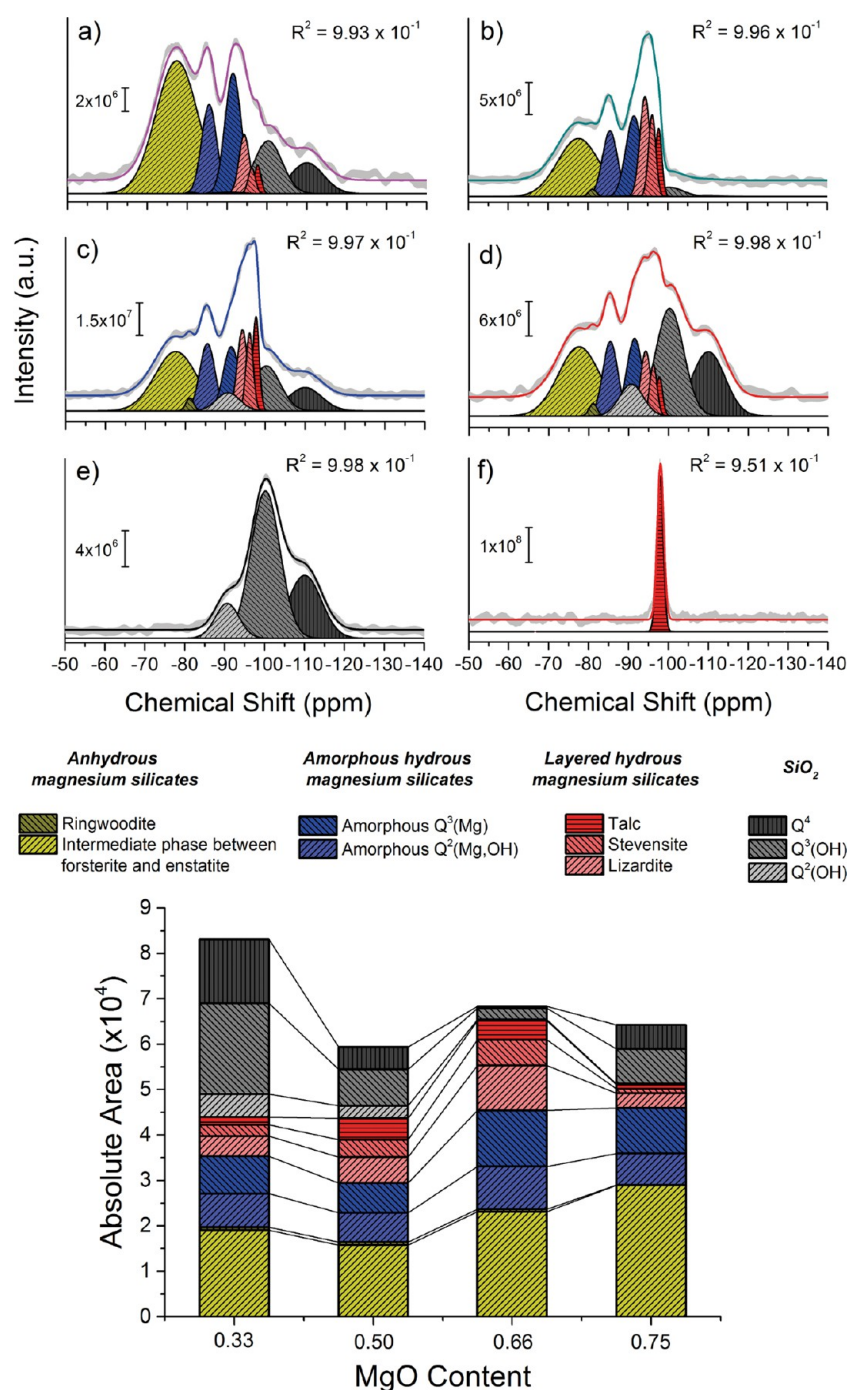


**Figure 7.** (top)  $^1\text{H}$ - $^{29}\text{Si}$  cross-polarized MAS NMR spectra and deconvoluted spectra of the  $\text{SiO}_2$ - $\text{MgO}$  (III)<sub>nano</sub> catalysts with different MgO content (a) 0.75, (b) 0.66, (c) 0.50, (d) 0.33, (e) 0 ( $\text{SiO}_2$ ), and (f) talc. (bottom) Absolute areas of magnesium silicate species identified in the  $^1\text{H}$ - $^{29}\text{Si}$  CP-MAS NMR data of the  $\text{SiO}_2$ - $n\text{MgO}$  (III)<sub>nano</sub> materials after deconvolution. Please see the text for a discussion on the assignments.

assignment of the signals at  $-85.5$  and  $-91.5$  to a set of (five) signals belonging to a calcined sepiolite, for which detailed data was reported by Caillerie et al.,<sup>53</sup> is discarded on the basis of differences in peak position and relative intensities.

This leaves the three signals shifted most downfield to  $-94.3$ ,  $-96.1$ , and  $-97.8$  to be assigned. These three signals, in contrast to the other silicates, actually increase significantly with increasing CP contact times. Such a behavior is also observed for the reference compound talc (Figure S6). Moreover, the 2D  $^1\text{H}$  detected CP-MAS  $^{29}\text{Si}$ - $^1\text{H}$  spectrum of the 0.50 MgO content sample shows rather sharp and strong  $^{29}\text{Si}$ - $^1\text{H}$

correlations at those frequencies (Figure 6). The cross-peak at  $-97.6$  ( $^{29}\text{Si}$ ) and  $0.75$  ( $^1\text{H}$ ) ppm can easily be assigned to talc, as it overlaps with the reference talc spectrum shown in red and is in line with literature.<sup>48</sup> The other two signals occur at slightly upfield  $^1\text{H}$  frequencies of  $0.55$  ( $-96.0$   $^{29}\text{Si}$ ) and  $0.40$  ( $-94.3$   $^{29}\text{Si}$ ) ppm, indicating further shielding of the protons. These proton chemical shifts are characteristic for structural hydroxyl atoms located in the hexagonal cavity of trioctahedral phyllosilicates.<sup>52</sup> The peak at  $-96.1$  ppm is now proposed to originate from a talc-like magnesium silicate and tentatively assigned to the silicate stevensite (i.e., defect site-containing

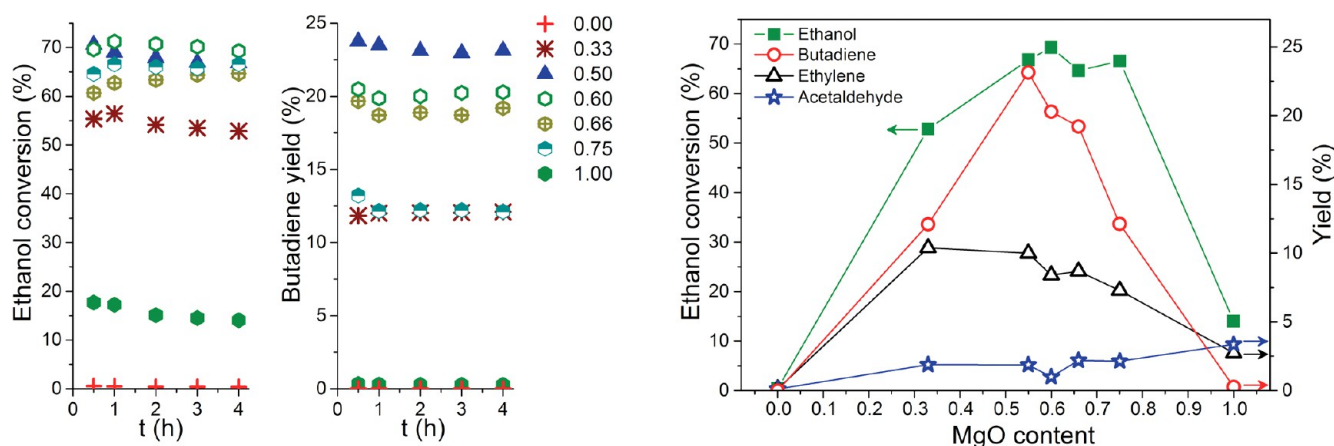


**Figure 8.** Comparison of the ethanol conversion (left), butadiene yield (center) and yield of the main products at 4 h time on stream (right) for  $\text{SiO}_2$ , MgO five  $\text{SiO}_2$ -MgO (III)<sub>nano</sub> catalysts having different nominal MgO content.

$\text{Mg}_x(\text{Mg}_{3-x}\square_x)\text{Si}_4\text{O}_{10}(\text{OH})_2$ .<sup>54</sup> In support, it was previously reported that, unlike natural talc, synthetic talc showed two signals, one at  $-97.3$  ppm and a satellite peak at  $-95.1$  ppm, arising from  $\text{Mg}^{2+}$  vacancies in the octahedral magnesium layer in stevensite.

Finally, the signal at  $-94.3$  ppm indicates the formation of hydrous phyllosilicate polymorphs of the serpentine-type ( $\text{Mg}_3\text{Si}_2\text{O}_5(\text{OH})_4$ ), such as antigorite, chrysotile, and lizardite for which characteristic peaks have been reported in the range of  $-93$  to  $-95$  ppm ( $-92.9$  ppm for chrysotile,<sup>37</sup>  $-93.7$  ppm for lizardite,<sup>55</sup>  $\sim -95$  ppm for antigorite,<sup>56</sup> respectively). Although Kvísl et al. previously reported that antigorite might be formed during wet-kneading<sup>9</sup> and Zhang and co-workers showed chrysotile to be the preferred polymorph in thermodynamic calculations,<sup>31,57</sup> we prefer to assign this signal to a lizardite-like silicate. Indeed, in a systematic investigation of  $\text{Mg}(\text{OH})_2$ - $\text{SiO}_2$ - $\text{H}_2\text{O}$  structures, blending  $\text{Mg}(\text{OH})_2$  slurry with silica fume, Walling et al. ruled out the formation of chrysotile and antigorite in  $\text{Mg}(\text{OH})_2$ - $\text{SiO}_2$ - $\text{H}_2\text{O}$  structures on the basis of their  $^{29}\text{Si}$  and  $^{25}\text{Mg}$  MAS NMR data. The magnesium silicate signal seen at  $-93.7$  ppm was assigned to a poorly crystalline lizardite-type silicate instead.<sup>55</sup> It should be noted that, expectedly, the CP efficiency differs with respect to the types of silicates that have now been assigned in the CP-MAS spectra. This is reflected in the different buildup curves seen for the different classes as a function of contact time (Figure S6). The amount of different magnesium silicates therefore cannot be compared in one and the same sample but can be compared *between* samples, providing the same CP contact time is used. Because CP buildup efficiency for layered hydrous magnesium silicates will be the same in the different samples, sensitization in signal areas can directly be related to an increase and/or decrease in the amount of the corresponding silicates. The latter intersample comparison is used below to correlate silicate speciation with catalytic performance (vide infra).

Summarizing, the CP-MAS NMR results suggest that (at least) five magnesium silicates are formed. These include two anhydrous species (mainly an intermediate phase between forsterite and enstatite and a minute amount of ringwoodite) and four hydrous silicates (an amorphous magnesium silicate, lizardite, stevensite and talc). Of the latter group, the layered hydrous magnesium silicates such as lizardite, stevensite, and talc are considered to contribute to the FT-IR bands at  $3672$ –

$3669\text{ cm}^{-1}$  (Figure 5). In addition, it was previously reported that amorphous magnesium silicates show the characteristic hydroxyl bands of magnesium silicates in the region of  $\sim 3740$ – $3700\text{ cm}^{-1}$ , depending on their preparation method.<sup>10,11</sup> The presence of (at least) three different magnesium silicates explains the position and broadness of FT-IR spectra of the samples with different MgO content. For example, as indicated by the FT-IR results (Figure 5), the  $\text{SiO}_2$ -MgO (III)<sub>nano</sub> material with 0.75 MgO content, possesses a limited amount of the layered hydrous magnesium silicates.

These structural insights can now be related to catalyst efficiency. The effect of relative MgO content on catalyst performance is shown in Figure 8. For the wet-kneaded catalysts, the acetaldehyde yield is quite similar, and the ethanol conversion levels fall in a quite narrow range of 64–69% after 4 h time on stream, with the 0.33 sample being the exception and showing only  $\sim 53\%$  conversion. The butadiene yields follow a volcano-shaped trend, with the 0.50 sample performing best. The results shown here agree well with those reported by Kitayama et al.;<sup>33</sup> the small difference in optimal MgO content (0.40 vs 0.50 observed here) for catalysis and in the absolute butadiene yield can be attributed to the considerable amount of NiO used in this literature example. Indeed, it is known that transition metal oxides can significantly alter the performance of ( $\text{SiO}_2$ -MgO) catalysts for the Lebedev process.<sup>5,6</sup> Notably, ethylene yields follow a (different) volcano curve with the silica-rich 0.33 MgO sample giving the highest ethylene amount. MgO showed a low, yet significant amount of ethylene, while the amount produced over  $\text{SiO}_2$  is negligible. That the  $\text{SiO}_2$ -MgO materials all produce more ethylene than MgO does, suggests that the magnesium silicates contain acid sites of sufficient acidity for ethanol dehydration.<sup>11</sup> Indeed, the variation in the relative amount of amorphous hydrous magnesium silicates in the catalyst series (determined as integrated area from the deconvoluted NMR spectra and scaled with number of scans) correlates linearly with ethylene yield (Figure 9). Note that while the differences in polarization transfer efficiency preclude determination of the absolute amounts of the various magnesium silicates, a relative comparison of the same magnesium silicates within the series of catalysts is possible. It is interesting to note that  $\text{SiO}_2$ -MgO materials prepared by coprecipitation (samples which also must consist of structurally ill-defined, amorphous magnesium

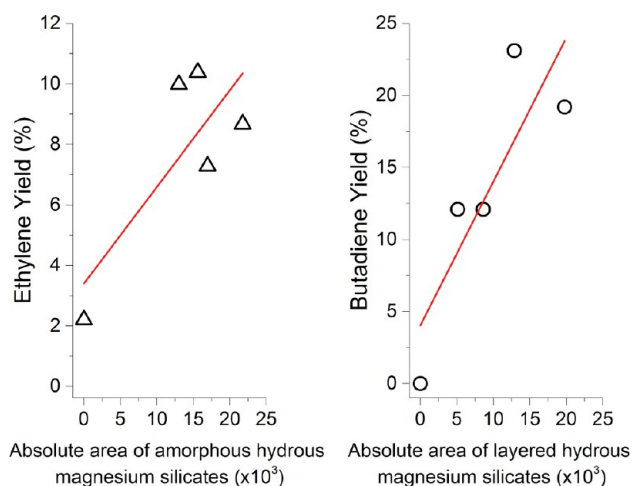


**Figure 9.** Ethylene and 1,3-butadiene yield as a function of absolute area detected for amorphous hydrous magnesium silicates and layered hydrous silicates, respectively. The areas were determined by scaling the integrals of the corresponding peaks with the number of scans. The data point  $x = 0$  is the  $\text{MgO}_{\text{nano}}$  sample (1.0 MgO content).

silicates) also showed high ethylene yields, as previously reported.<sup>11</sup>

Taking catalytic performance and the CP-MAS NMR results into account, the ratio between the right magnesium silicates and MgO in the 0.50 sample is apparently best for butadiene production. As already mentioned above, Kitayama et al. also proposed the best catalyst in their series to be the one in which a layered nickel magnesium silicate coexists with a small amount of MgO.<sup>33</sup> The CP-MAS NMR results now suggest the hydrous layered magnesium silicates to be most relevant for butadiene production. In fact, the increase in amount of lizardite, stevensite, and talc (depicted as absolute areas, to take into account CP efficiency, see above) correlates linearly with the butadiene yield (Figure 9). These layered magnesium silicates thus must, together with the strongly basic MgO component, be mainly responsible for the proper balance in acidic/basic sites required for butadiene production. Indeed, according to the literature, talc has both acidic<sup>58</sup> and basic sites,<sup>59</sup> with the latter study showing lizardite to be more basic than talc. Lizardite, which consists of an octahedral  $\text{Mg}^{2+}$  layer bridged with tetrahedral  $\text{Si}^{4+}$  cation layers (O:T), has octahedral surface Mg species perturbed by the inner Si layer; talc, on the other hand consists of an octahedral  $\text{Mg}^{2+}$  layer sandwiched by two tetrahedral  $\text{Si}^{4+}$  cation layers (T:O:T) and has mostly exposed tetrahedral Si species at the surface, in this case perturbed by the inner octahedral Mg layer. The silicates thus present different surface sites that can be involved in various steps of the ethanol-to-butadiene Lebedev process. Further studies are now needed to get more insight into how each of the hydrous magnesium silicates contribute to the acidic and basic properties for butadiene formation, as well as the role of each in the individual reaction steps.

## 5. CONCLUSIONS

Wet-kneading is a rather nonconventional method for the preparation of catalytic materials on a laboratory or industrial scale. This preparation method nonetheless elicits chemical and structural changes in  $\text{SiO}_2\text{--MgO}$  materials that makes them perform best in the Lebedev reaction. To better understand the unique structural consequences of wet-kneading, we studied the

effect of variation of Mg precursor and of MgO content on catalyst structure and, consequently, on performance. Most importantly, the nature and the amount of magnesium silicates that are formed as a function of preparation parameter are demonstrated to be key to catalyst performance. Accordingly, variation of the Mg precursor at fixed MgO content showed that the catalyst possessing the highest amount of magnesium silicates, as estimated from the TEM and FT-IR data, gave the highest butadiene yield. In turn, variation of the MgO content with a fixed Mg precursor showed a volcano-shaped dependence of the butadiene yield, with the 0.50 sample performing best. Taking this and the essential role of the magnesium silicates into account, we thus propose the ratio of magnesium silicates to MgO, which is required for its specific basicity, to be key for catalysis, with any  $\text{SiO}_2$  remaining in the catalyst after wet-kneading to be catalytically inert. Analysis of the  $\text{SiO}_2\text{--MgO (III)}_{\text{nano}}$  catalysts with different MgO content with CP-MAS NMR spectroscopy allowed for several different magnesium silicates to be identified including anhydrous magnesium silicates, amorphous hydrous as well as the layered hydrous magnesium silicates. Taken together, catalyst characterization results suggest that the hydrous magnesium silicate phases are catalytically most relevant; in particular, the amounts of layered magnesium silicates (lizardite, stevensite, and talc) were found to correlate with butadiene yield. The insights thus gained in the structural requirements for efficient butadiene production can now aid in the synthesis of better catalysts, perhaps by other synthetic means than wet-kneading.

## ■ ASSOCIATED CONTENT

### ● Supporting Information

The Supporting Information is available free of charge on the ACS Publications website at DOI: 10.1021/acscatal.5b02972.

Schematic representation of 2D  $^1\text{H}$  detected  $^{29}\text{Si}\text{--}^1\text{H}$  CP-MAS NMR and 2D CP-MAS NMR spectra of  $\text{SiO}_2\text{--MgO (III)}_{\text{nano}}$  sample with 0.50 MgO content; SEM images of  $\text{Mg(OH)}_2$  precursors of  $\text{SiO}_2\text{--MgO (III)}$  and  $\text{SiO}_2\text{--MgO (III)}_{\text{nano}}$ ; pH variation during wet-kneading of  $\text{SiO}_2\text{--MgO (III)}_{\text{nano}}$  with 0.50 MgO content; XRD patterns of  $\text{SiO}_2\text{--MgO (III)}_{\text{nano}}$  with different MgO content; summary of the  $^1\text{H}\text{--}^{29}\text{Si}$  CP-MAS NMR data of  $\text{SiO}_2\text{--MgO (III)}_{\text{nano}}$  after deconvolution and  $^1\text{H}\text{--}^{29}\text{Si}$  CP-MAS NMR spectra of  $\text{SiO}_2\text{--MgO (III)}_{\text{nano}}$  with 0.50 MgO content at different CP contact times (PDF)

## ■ AUTHOR INFORMATION

### Corresponding Authors

\*E-mail for B.M.W.: [b.m.weckhuysen@uu.nl](mailto:b.m.weckhuysen@uu.nl).

\*E-mail for P.C.A.B.: [p.c.a.bruijnincx@uu.nl](mailto:p.c.a.bruijnincx@uu.nl).

### Author Contributions

<sup>§</sup>These authors (S.-H. Chung and C. Angelici) contributed equally.

### Notes

The authors declare no competing financial interest.

## ■ ACKNOWLEDGMENTS

This research was performed within the framework of the CatchBio program. The authors gratefully acknowledge the support of the Smart Mix Program of The Netherlands Ministry of Economic Affairs, and The Netherlands Ministry of Education, Culture and Science and NWO for funding of the NMR infrastructure (Middelgroot program, grant number



700.58.102). We thank Prof. Erik Heeres (University of Groningen) for the ICP measurements. Johan van der Zwan is acknowledged for NMR technical support.

## REFERENCES

- (1) Bruijninx, P. C. A.; Weckhuysen, B. M. *Angew. Chem., Int. Ed.* **2013**, *52*, 11980–11987.
- (2) Sushkevich, V. L.; Ivanova, I. I.; Ordonsky, V. V.; Taarning, E. *ChemSusChem* **2014**, *7*, 2527–2536.
- (3) De Baerdemaeker, T.; Feyen, M.; Müller, U.; Yilmaz, B.; Xiao, F.-S.; Zhang, W.; Yokoi, T.; Bao, X.; Gies, H.; De Vos, D. E. *ACS Catal.* **2015**, *5*, 3393–3397.
- (4) Sushkevich, V. L.; Palagin, D.; Ivanova, I. I. *ACS Catal.* **2015**, *5*, 4833–4836.
- (5) Angelici, C.; Weckhuysen, B. M.; Bruijninx, P. C. A. *ChemSusChem* **2013**, *6*, 1595–1614.
- (6) Makshina, E. V.; Dusselier, M.; Janssens, W.; Degre, J.; Jacobs, P. A.; Sels, B. F. *Chem. Soc. Rev.* **2014**, *43*, 7917–7953.
- (7) Natta, G.; Rigamonti, R. *Chim. Ind.* **1947**, *29*, 239–243.
- (8) Ohnishi, R.; Akimoto, T.; Tanabe, K. *J. Chem. Soc., Chem. Commun.* **1985**, 1613–1614.
- (9) Kvisle, S.; Agüero, A.; Sneed, R. P. A. *Appl. Catal.* **1988**, *43*, 117–131.
- (10) Angelici, C.; Velthoen, M. E. Z.; Weckhuysen, B. M.; Bruijninx, P. C. A. *ChemSusChem* **2014**, *7*, 2505–2515.
- (11) Angelici, C.; Velthoen, M. E. Z.; Weckhuysen, B. M.; Bruijninx, P. C. A. *Catal. Sci. Technol.* **2015**, *5*, 2869–2879.
- (12) Zhang, M.; Gao, M.; Chen, J.; Yu, Y. *RSC Adv.* **2015**, *5*, 25959–25966.
- (13) Janssens, W.; Makshina, E. V.; Vanelderen, P.; De Clippel, F.; Houthoofd, K.; Kerkhofs, S.; Martens, J. A.; Jacobs, P. A.; Sels, B. F. *ChemSusChem* **2015**, *8*, 994–1008.
- (14) Makshina, E. V.; Janssens, W.; Sels, B. F.; Jacobs, P. A. *Catal. Today* **2012**, *198*, 338–344.
- (15) Niiyama, H.; Morii, S.; Echigoya, E. *Bull. Chem. Soc. Jpn.* **1972**, *45*, 655–659.
- (16) Lewandowski, M.; Babu, G. S.; Vezzoli, M.; Jones, M. D.; Owen, R. E.; Mattia, D.; Plucinski, P.; Mikolajska, E.; Ochendusko, A.; Apperley, D. C. *Catal. Commun.* **2014**, *49*, 25–28.
- (17) Kitayama, Y.; Michishita, A. *J. Chem. Soc., Chem. Commun.* **1981**, *9*, 401–402.
- (18) Gruver, V.; Sun, A.; Fripiat, J. J. *Catal. Lett.* **1995**, *34*, 359–364.
- (19) Vatsha, B.; Tetyana, P.; Shumbula, P. M.; Ngila, J. C.; Sikhivihulu, L. M.; Moutloali, R. M. *J. Biomater. Nanobiotechnol.* **2013**, *4*, 365–373.
- (20) Fung, B. M.; Khitrin, A. K.; Ermolaev, K. J. *Magn. Reson.* **2000**, *142*, 97–101.
- (21) Weingarth, M.; Van Der Cruysen, E. A. W.; Ostmeier, J.; Lievestro, S.; Roux, B.; Baldus, M. J. *Am. Chem. Soc.* **2014**, *136*, 2000–2007.
- (22) Zhou, D. H.; Rienstra, C. M. *J. Magn. Reson.* **2008**, *192*, 167–172.
- (23) Vansant, E. F.; Van Der Voort, P.; Vrancken, K. C. *Characterization and Chemical Modification of the Silica Surface*; Elsevier Science: Amsterdam, 1995.
- (24) Knözinger, E.; Jacob, K.-H.; Singh, S.; Hofmann, P. *Surf. Sci.* **1993**, *290*, 388–402.
- (25) RRUFF Database Homepage. <http://rruff.info/antigorite> (accessed Sep 15, 2015).
- (26) RRUFF Database Homepage. <http://rruff.info/talc> (accessed Sep 15, 2015).
- (27) RRUFF Database Homepage. <http://rruff.info/lizardite> (accessed Sep 15, 2015).
- (28) Choi, I.; Smith, R. W. *J. Colloid Interface Sci.* **1972**, *40*, 253–262.
- (29) Busey, R. H.; Mesmer, R. E. *Inorg. Chem.* **1977**, *16*, 2444–2450.
- (30) Demadis, K. D. *The science and technology of industrial water treatment*; Amjad, Z., Ed.; IWA Publishing /CRC Press: London, Boca Raton, 2010.
- (31) Li, Z.; Zhang, T.; Hu, J.; Tang, Y.; Niu, Y.; Wei, J.; Yu, Q. *Constr. Build. Mater.* **2014**, *61*, 252–259.
- (32) Büttner, W.; Saager, R. *TMPM, Tschermaks Mineral. Petrogr. Mitt.* **1982**, *30*, 177–187.
- (33) Kitayama, Y.; Satoh, M.; Kodama, T. *Catal. Lett.* **1996**, *36*, 95–97.
- (34) Rohl, A. N.; Langer, A. M. *Environ. Health Perspect.* **1974**, *9*, 95–109.
- (35) Rinaudo, C.; Gastaldi, D.; Belluso, E. *Can. Mineral.* **2003**, *41*, 883–890.
- (36) Trittschack, R.; Grobety, B.; Koch-Müller, M. *Am. Mineral.* **2012**, *97*, 1965–1976.
- (37) Mackenzie, K. J. D.; Meinhold, R. H. *Am. Mineral.* **1994**, *79*, 43–50.
- (38) Temuujin, J.; Okada, K.; MacKenzie, K. J. D. *J. Solid State Chem.* **1998**, *138*, 169–177.
- (39) Dumas, A.; Martin, F.; Le Roux, C.; Micoud, P.; Petit, S.; Ferrage, E.; Brendlé, J.; Grauby, O.; Greenhill-Hooper, M. *Phys. Chem. Miner.* **2013**, *40*, 361–373.
- (40) Griffin, J. M.; Berry, A. J.; Frost, D. J.; Wimperis, S.; Ashbrook, S. E. *Chem. Sci.* **2013**, *4*, 1523.
- (41) Carlson, E. T.; Peppler, R. B.; Wells, L. S. *J. Res. Natl. Bur. Stand.* (1934) **1953**, *51*, 179–184.
- (42) Chen, L.; Ye, G.; Zhou, W.; Dijkman, J.; Sels, B.; Malfliet, A.; Guo, M. *Ceram. Int.* **2015**, *41*, 12651–12657.
- (43) Magi, M.; Lippmaa, E.; Samoson, A.; Engelhardt, G.; Grimmer, A.-R. *J. Phys. Chem.* **1984**, *88*, 1518–1522.
- (44) Park, D. G.; Duchamp, J. C.; Duncan, T. M.; Burlitch, J. M. *Chem. Mater.* **1994**, *6*, 1990–1995.
- (45) Sindorf, D.; Maciel, G. J. *Phys. Chem.* **1982**, *86*, 5208–5219.
- (46) Maciel, G. E.; Sindorf, D. W. *J. Am. Chem. Soc.* **1980**, *102*, 7606–7607.
- (47) Sen, T.; Bruce, I. J. *Sci. Rep.* **2012**, *2*, 1–6.
- (48) MacKenzie, K. J. D.; Bradley, S.; Hanna, J. V.; Smith, M. E. *J. Mater. Sci.* **2013**, *48*, 1787–1793.
- (49) Stebbins, J. F.; Panero, W. R.; Smyth, J. R.; Frost, D. J. *Am. Mineral.* **2009**, *94*, 626–629.
- (50) Haiber, M.; Ballone, P.; Parrinello, M. *Am. Mineral.* **1997**, *82*, 913–922.
- (51) d'Espinose de la Caillerie, J.-B.; Kermarec, M.; Clause, O. *J. Phys. Chem.* **1995**, *99*, 17273–17281.
- (52) Alba, M. D.; Becerro, A. I.; Castro, M. A.; Perdigon, A. C. *Chem. Commun.* **2000**, 37–38.
- (53) Caillerie, J.-B. D.; Fripiat, J. J. *Clay Miner.* **1994**, *29*, 313–318.
- (54) Chabrol, K.; Gressier, M.; Pebere, N.; Menu, M.-J.; Martin, F.; Bonino, J.-P.; Marichal, C.; Brendle, J. *J. Mater. Chem.* **2010**, *20*, 9695.
- (55) Walling, S. A.; Kinoshita, H.; Bernal, S. A.; Collier, N. C.; Provis, J. L. *Dalt. Trans.* **2015**, *44*, 8126–8137.
- (56) Nakata, S.; Asaoka, S.; Kondoh, T.; Takahashi, H. *Nendo Kagaku* **1986**, *26*, 197–208.
- (57) Zhang, T.; Cheeseman, C. R.; Vandeperre, L. J. *Cem. Concr. Res.* **2011**, *41*, 439–442.
- (58) Wu, D. Y.; Matsue, N.; Henmi, T.; Yoshinaga, N. *Clay Sci.* **1993**, *8*, 367–379.
- (59) Sivaiah, M. V.; Robles-Manuel, S.; Valange, S.; Barrault, J. *Catal. Today* **2012**, *198*, 305–313.